An Improved Discharge Profile-Based DC-Link Capacitance Estimation for Traction Inverter in Electric Vehicle Applications

Xing Wei, *Student Member, IEEE*, Bo Yao, *Graduate Student Member, IEEE*, Yingzhou Peng, *Senior Member, IEEE*, Yongchao Sun, Kai Wang, *Member, IEEE*, and Huai Wang, *Senior Member, IEEE*

***Abstract*—DC-link capacitor is an important part of traction inverters in electric vehicles (EVs), contributing to cost, size, and failure rate on a considerable scale. This article proposes a noninvasive dc-link capacitance estimation method based on the capacitor discharge profile during the turning-OFF transition of a traction inverter. The proposed method relies on the existing control and measurement of the traction inverter without the need for software modifications and hardware updates. It minimizes the new risks introduced into the system operation because the estimation procedure is implemented after vehicles are parked. A novel correction solution is proposed to secure the estimation accuracy while also reducing the sampling requirements. Compared with conventional estimation methods, the proposed scheme outperforms in complexity and accuracy. The proof-of-concept experiments based on a scaled-down inverter prototype and a full-scale traction inverter for EV applications verify the feasibility of the proposed method.**

***Index Terms*—Capacitance estimation, condition monitoring, dc-link capacitor, electric vehicle (EV), traction inverter.**

I. Introduction

DC-LINK capacitor is a critical component of traction inverters, which smooths the dc-link voltage variation, absorbs the high-frequency harmonics, and balances the instantaneous power difference between the front-end power supply and the rear-end electric machine (EM) [1], [2], [3]. However, due to the harsh operating and environmental conditions in practice, the dc-link capacitor can be fragile after a long-term operation, and its capability to withstand thermal and electrical stresses can be deteriorated [3], [4], [5], [6], [7]. As reported in [7], about 30% of the failures in power electronic converters are caused by the capacitor, which has been considered one of the most vulnerable components. From this point of view, it is essential to monitor the operating and health status of the dc-link capacitor to ensure reliable field operation, and consequently, the optimal operation and maintenance can be performed proactively before failure occurs [7], [8], [9].

Condition monitoring is implemented by utilizing health indicators that are sensitive to component degradation [10], [11]. In the case of capacitors, it is widely reported that the equivalent series resistance (ESR) is commonly used to monitor the aluminum electrolytic capacitor, while the capacitance value is applicable for any type of capacitor [3]. For applications like traction inverters in electric vehicles (EVs), where the dc-link is typically designed with film capacitors [5], capacitance is the preferred health indicator. Therefore, over the last two decades, tremendous efforts have been made to the dc-link capacitance estimation for traction inverter applications [11], as shown in Table I, and these existing studies primarily fall into three categories: capacitor ripple-based, external signal injection-based, and charge/discharge profile-based methods.

1) Capacitor Ripple-Based Methods: According to Ohm's law, the capacitor capacitance can be estimated by periodic ripples. In [12], the voltage and current ripples of the dc-link capacitor in traction inverters are directly measured by sensors, and the Goertzel algorithm is applied to extract the low-frequency components to estimate the capacitance. To avoid using a current transducer in series with the dc-link capacitor, Rodrigues et al. [13] and Zhang et al. [14] acquired the capacitor current indirectly by the difference between the input current of the traction inverter and the input current of the power semiconductor module. However, the estimation results present a low accuracy level with an error of up to 5.4 % due to current measurement errors and system noise, and a measurement system with a high sampling rate is required to capture ripple components.

2)External Signal Injection-Based Methods: The implementation of external signal injection-based methods is to inject a perturbation signal into the whole power converter, and then utilize algorithms to analyze the voltage and current induced on the dc-link capacitor to estimate the capacitance. In [15] and [16], a controlled ac voltage or current signal is injected into an ac/dc/ac power converter during normal operation, and the

Manuscript received 20 September 2023; revised 24 December 2023 and 19 February 2024; accepted 22 March 2024. Date of publication 1 April 2024; date of current version 16 May 2024. Recommended for publication by Associate Editor M. Hartmann. *(Corresponding author: Bo Yao.)*

Xing Wei, Bo Yao, and Huai Wang are with the Department of Energy, Aalborg University, 9220 Aalborg, Denmark (e-mail: xwe@energy.aau.dk; ybo@energy.aau.dk; hwa@energy.aau.dk).

Yingzhou Peng is with the School of Electrical Engineering, Hunan University, Hunan 410012, China (e-mail: yzpeng@hnu.edu.cn).

Yongchao Sun and Kai Wang are with the NIO Inc., Shanghai 201804, China (e-mail: yongchao.sun1@nio.com; kai.wang@nio.com).

Color versions of one or more figures in this article are available at https://doi.org/10.1109/TPEL.2024.3383153.

Digital Object Identifier 10.1109/TPEL.2024.3383153

TABLE I
CLASSIFICATION OF DC-LINK CAPACITANCE ESTIMATION METHODS FOR TRACTION INVERTER APPLICATIONS

Method	Working Principle	Advantage	Limitation	
Capacitor ripple-based methods	**[12]:** A current transducer is used to measure the capacitor current, and the ripples are extracted by a digital filter implemented by the Goertzel algorithm	High estimation accuracy	1. Require complex algorithms 2. High requirements for sampling accuracy and rate 3. Introduce new risks to system operation	Require additional current sensors
	[13], [14]: Capture capacitor current ripple indirectly with front-end and rear-end currents	No additional hardware		High estimation error of up to 5.4 % due to measurement errors and system noise
External signal injection-based methods	**[15], [16]:** Inject AC voltage or current into the DC-link via the front-end AC/DC converter, then use algorithms to analyze induced voltage or power ripple	1. No additional hardware 2. High estimation accuracy	1. Require control modification and complex algorithms 2. High requirements for sampling accuracy and rate 3. Introduce new risks to system operation	
	[17]: Inject load motor current into the DC-link by varying gate driving, and the capacitance is estimated from the voltage rise and load current			
Charge/discharge profile-based methods	**[18]:** DC-link capacitor is discharged via an auxiliary electric network consisting of switches and resistors	1. No operation interference 2. No need for complex algorithms	1. Require additional hardware and control software 2. Variations in the impedance of auxiliary networks and filters can affect estimation accuracy 3. Increased costs and additional reliability issues	
	[19]: DC-link capacitor is charged via an *LCR* network consisting of the impedance network of the traction inverter and an auxiliary braking rheostat			
	[20]: DC-link capacitor is discharged via an *LC* resonant network consisting of two-phase motor stator windings	1. No operation interference 2. No need for additional hardware and complex algorithms	1. Require additional control software [20] 2. Discharge through two-phase motor stator winding discharge inevitably induces torque in the load motor [20] 3. High requirements for sampling accuracy, synchronization, position, and rate 4. High estimation error of up to 5.1 % due to measurement errors and non-ideal switching characteristics of power semiconductor	
	[21], [22]: DC-link capacitor is discharged through three-phase motor stator windings			

resulting voltage or power ripple induced on the dc-link capacitor is analyzed by fast-recursive and recursive least squares algorithms to realize the capacitance estimation. Notice that these methods are not suitable for traction inverters with an uncontrolled rectifier or battery pack connected to the front end. Therefore, Meng and Zhang [17] proposed a scheme to inject the load motor current of a particular phase into the dc-link of the traction inverter.

External signal injection-based methods typically allow for high-accuracy estimation without the need for additional sensors. Nevertheless, they require control software modifications and complex algorithms, and still have a high requirement for sampling in terms of accuracy and rate, which significantly increases the estimation complexity and could be unacceptable in practical applications. In addition, whether the methods rely on capacitor ripple or external signal injection, they are performed during the operation of the traction inverter, which can pose a potential threat to operational safety.

3) Charge/Discharge Profile-Based Methods: To minimize the new risks introduced to the system operation, several works have been devoted to estimating the capacitance from the discharge or charge profiles of the dc-link capacitor during the shutdown or start-up process of the traction inverter. In [18], an auxiliary discharge network consisting of power devices and resistors is proposed in parallel with the dc-link capacitor, and the capacitance is estimated by the resistance value of the auxiliary resistor net and the time constant extracted from the discharge profile. In [19], an *LCR* charge network formed by the dc chock and dc-link capacitor in the traction inverter and an auxiliary braking rheostat is proposed, and capacitance is identified by the network response during stable charging. However, it is worth noting that these methods are strongly reliant on the impedance parameters of the auxiliary electric network and the traction inverter, and as a result, the variation in operating and environmental conditions can affect the estimation accuracy. Moreover, the power devices in these auxiliary electric networks can lead to increased costs and additional reliability issues.

Besides the additional discharging path, the motor stator windings in traction systems can also be used to form the discharge loop when the motor is stopped. In [20], an *LC*-resonant discharge circuit consisting of the dc-link capacitor and two-phase stator windings is proposed after the traction inverter is disconnected from the front-end power supply. However, this method is software-invasive and complex, requiring an additional resonant current control and a high current sampling rate, and the two-phase winding discharge will inevitably cause torque in the load motor in practice due to the nonideal current control. The estimation schemes presented in [21] and [22] utilizing three-phase motor stator windings can solve the load torque issue to some extent and they can be implemented with the existing sensors and control of the traction inverter. The major drawbacks of these schemes are the high requirements

for sampling synchronization and position to calculate the capacitor discharge current, i.e., the sampling frequency should be not lower than the switching frequency and the three-phase stator current needs to be sampled synchronously at the peak or valley of the pulsewidth modulation (PWM) carrier. In practical traction inverters, however, these sampling requirements could be difficult to fulfill as their measurement system is typically designed for control purposes, where the converter signals are measured asynchronously in the vicinity of the peak or valley of the PWM carrier and the sampling frequency could be lower than the switching frequency. In addition, the estimation accuracy of these schemes could deteriorate in field applications as the signal errors caused by nonideal sampling conditions and semiconductor switching characteristics are inevitable and have a significant impact on the estimation accuracy.

This article proposes an application-oriented dc-link capacitance estimation method for traction inverters, which is also achieved through the dc-link discharging operation mode of the traction inverter. Different from the existing methods, a novel error correction solution is proposed in this article to eliminate and compensate for signal errors, thus improving the estimation accuracy in field applications. In addition, by exploiting the discharge steady-state characteristics, the requirements for sampling rate, position, accuracy, and synchronization are greatly reduced, and as a result, there is no need to update the existing measurement platform. The proposed method is promising for EV applications as the required operation mode is an inherent and frequent activity, and it is expected to facilitate the practical implementation of health and condition monitoring for dc-link capacitors. The methodology feasibility is verified on both a scaled-down inverter prototype and a full-scale EV traction inverter.

The rest of this article is organized as follows. Section II introduces the dc-link discharge of traction inverters through the motor stator windings and presents the principles of the discharge profile-based capacitance estimation. Section III analyzes the sources of estimation errors and gives the correction solutions in practical implementations. Section IV gives the proof-of-concept of the proposed method based on experimental testing. Finally, Section V concludes this article.

II. Discharge Profile-Based DC-Link Capacitance Estimation

A. DC-Link Discharge Through Motor Stator Windings

The typical electrical configuration of the traction inverter in EVs is shown in Fig. 1, consisting of a dc-link capacitor, power semiconductor module, EM, and controller. Its front end is connected to the battery pack through circuit breakers, and the back-end EM can be either an ac induction machine or ac permanent magnet type [23]. The dc-link of the EV traction inverter is typically designed with film capacitors due to their high ripple current capability, high power density as well as low cost, and a simplified model of the dc-link capacitor is given in Fig. 1, where C and $R_{\rm s}$ represent the capacitance and ESR, respectively. To achieve high operating power, the current automotive power semiconductor module commonly uses insulated-gate bipolar transistors (IGBTs), which are expected to be replaced by silicon carbide (SiC) and gallium nitride (GaN) devices in the future to further reduce power loss and system size [5].

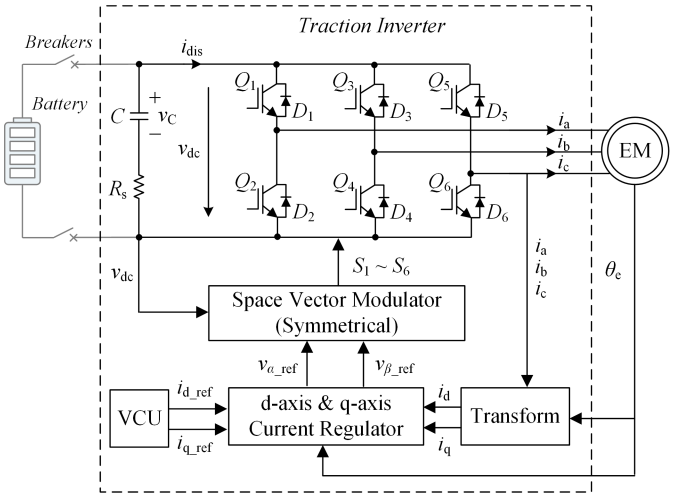

Fig. 1. Electrical configuration of the traction inverter for EV applications. C and $R_{\rm s}$ are the capacitance and ESR of the dc-link capacitor, Q_1 - Q_6 and D_1 - D_1 represent the IGBT devices and free-wheeling diodes, respectively. VCU is the vehicle control unit, and EM is the EM.

For safety reasons, after the vehicle is parked and shut down, the circuit breakers in Fig. 1 are opened to disconnect the traction inverter from the battery pack, followed by a pair of current commands $i_{\rm d\_ref}$ and $i_{\rm q\_ref}$ in the rotor flux reference frame issued from the vehicle control unit (VCU) to discharge the dc-link of the traction inverter [24]. Under the existing inner-loop current control and modulation strategy (typically symmetrical space vector PWM [5], [25]), the dc-link capacitor is discharged through the power semiconductor devices and the back-end motor stator windings according to the current references $i_{\rm d\_ref}$ and $i_{\rm q\_ref}$ and the rotor electrical angle $\theta_{\rm e}$. The d-axis current reference $i_{\rm d\_ref}$ is generally fixed and determined by the discharge time requirement, while the q-axis current reference $i_{\rm q\_ref}$ must be set to null to avoid torque generation. The rotor electrical angle $\theta_{\rm e}$ is fixed in a discharge, which is random and determined by the parking profile for traction inverters with synchronous motors, while for traction inverters with asynchronous motors, it can be set arbitrarily.

Fig. 2 gives a typical discharge profile of the dc-link capacitor in EV traction inverters with the initial dc-link voltage $V_{\rm C0}$ of 400 V, d-axis current reference $i_{\rm d\_ref}$ of 100 A, and rotor electrical angle $\theta_{\rm e}$ of $\pi/12$. It can be seen that the dc-link voltage $v_{\rm dc}$ decreases gradually in the discharge, and the three-phase stator current has fixed polarity due to the constant rotor electrical angle and reaches a steady state after a short transient. The steady-state value of the three-phase stator current is determined by both the current reference $i_{\rm d\_ref}$ and the rotor electrical angle $\theta_{\rm e}$, e.g., $i_{\rm a} = i_{\rm d\_ref}$*cos($\theta_{\rm e}$), and the duty cycles of the three-phase upper switches within the steady-state interval are around 50 % due to the low-amplitude output voltage vector in space vector modulation. The discharge is concluded when the dc-link voltage $v_{\rm dc}$ falls below a safety voltage (e.g., 36 V).

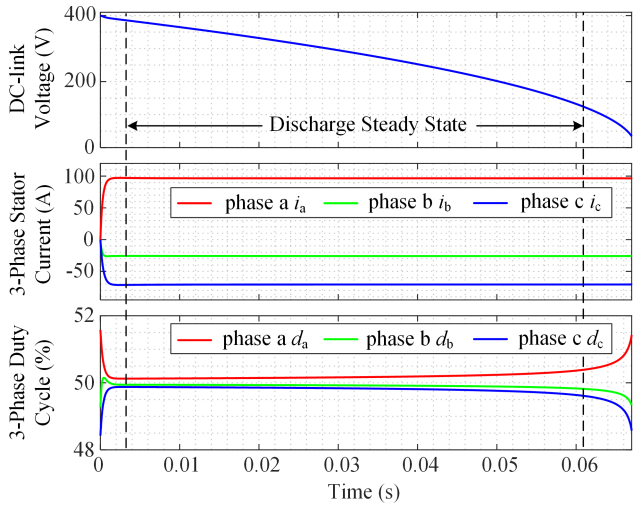

Fig. 2. Typical discharge profile of the DC-link capacitor in traction inverters with the initial dc-link voltage V_{C0} of 400 V, current reference i_{d_ref} of 100 A, and rotor electrical angle θ_e of $\pi/12$. d_a, d_b, and d_c stand for the duty cycles of the three-phase upper switches.

B. Principles of DC-Link Capacitance Estimation

According to Ohm's law, the capacitance C of the dc-link capacitor in Fig. 1 can be estimated through the capacitor discharge current i_{dis} and the capacitor voltage v_C as

$$C = \frac{\int_{t_0}^{t_0+\triangle t} i_{dis} dt}{\triangle v_C} \tag{1}$$

where $\triangle t$ is the estimation interval, and $\triangle v_C$ is the capacitor voltage drop over the estimation interval. Since the capacitor discharge current i_{dis} is always positive during the dc-link discharge, the integral term in (1) can be rewritten as

$$C = \frac{i_{dis\_ave} \triangle t}{\triangle v_C} \tag{2}$$

where i_{dis_ave} represents the average capacitor discharge current over the estimation interval.

Fig. 3 gives the key waveforms within the ith switching period t_0–t_8 of the discharge profile shown in Fig. 2, where S_a, S_b, and S_c stand for the driving signals of the three-phase upper switches, T_{a_i}, T_{b_i}, and T_{c_i} are the conduction times of the upper switches in the ith switching period, and τ_{a_i}, τ_{b_i}, and τ_{0_i} are the on-times of the switching vectors in space vector modulation. v_{dc_i}, i_{a_i}, i_{b_i}, and i_{c_i} are the dc-link voltage and three-phase stator current measured in the ith switching period, respectively, which are typically expected to be sampled at the peak or valley of the PWM carrier. Since the capacitor discharge current i_{dis}, as well as the voltage drop across the capacitor ESR, is zero at the sampling instant, the measured dc-link voltage v_{dc_i} is the required capacitor voltage.

The capacitor discharge current i_{dis} required for capacitance estimation cannot be measured directly in practical applications, but it can be calculated from the three-phase stator current and driving signals. Assuming that the three-phase driving signals S_a, S_b, and S_c is "1" when the upper switch is ON and "0" when the lower switch is on, the instantaneous capacitor discharge current i_{dis} can be presented as

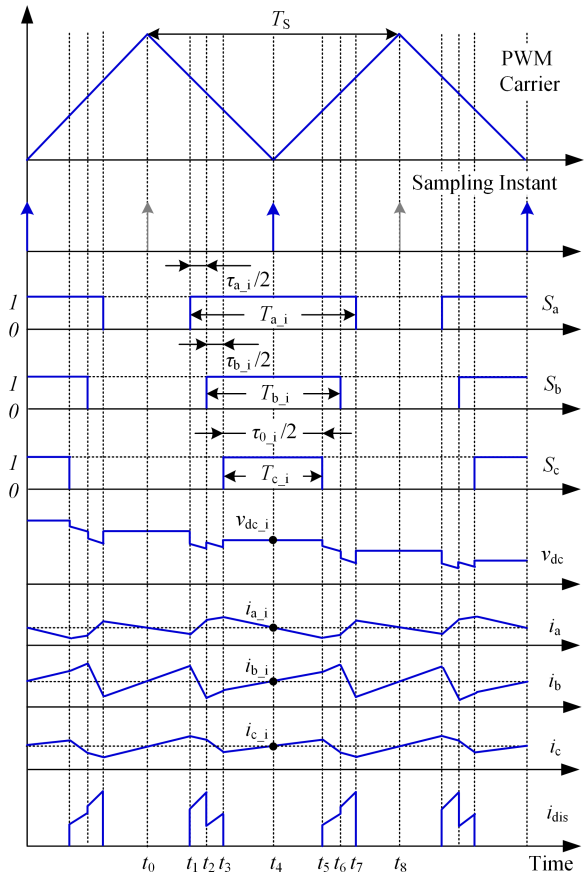

Fig. 3. Key waveforms of the traction inverter in the ith switching period of the discharge with the rotor electrical angle θ_e of $\pi/12$. T_S is the switching period, S_a, S_b, and S_c are the driving signals of the upper switches in each phase leg, T_{a_i}, T_{b_i}, and T_{c_i} are the conduction times of the upper switches, τ_{a_i}, τ_{b_i}, and τ_{0_i} are the switching vector on-times, v_{dc_i}, i_{a_i}, i_{b_i}, and i_{c_i} are the dc-link voltage and three-phase stator current measured in the ith switching period.

$$i_{dis} = S_a i_a + S_b i_b + S_c i_c. \tag{3}$$

By integrating (3) over the interval t_0 – t_8, the average discharge current $i_{dis\_ave\_i}$ over the ith switching period is given by

$$\begin{aligned} i_{dis\_ave\_i} &= \frac{1}{T_S}\int_{t_0}^{t_8} i_{dis} dt \\ &= \frac{\int_{T_{a\_i}} i_a dt}{T_S} + \frac{\int_{T_{b\_i}} i_b dt}{T_S} + \frac{\int_{T_{c\_i}} i_c dt}{T_S}. \end{aligned} \tag{4}$$

From Fig. 3, it can be known that the three-phase stator current is symmetrical within one switching period. Hence, the measured currents i_{a_i}, i_{b_i}, and i_{c_i} can be considered as the average values of the stator currents over their corresponding conduction intervals T_{a_i}, T_{b_i}, and T_{c_i}, and then the average capacitor discharge current $i_{dis\_ave\_i}$ in (4) can be calculated as

$$i_{dis\_ave\_i} = i_{a\_i} d_{a\_i} + i_{b\_i} d_{b\_i} + i_{c\_i} d_{c\_i} \tag{5}$$

where d_{a_i}, d_{b_i}, and d_{c_i} are the duty cycles of the three-phase upper switches in the ith switching period. Assuming that the

estimation interval includes n switching periods, the average discharge current $i_{\mathrm{dis\_ave}}$ of the dc-link capacitor over the entire estimation interval is given by

$$\begin{aligned} i_{\mathrm{dis\_ave}} &= \frac{1}{n}\sum_{i=1}^{n} i_{\mathrm{dis\_ave\_i}} \\ &= \frac{1}{n}\sum_{i=1}^{n}\left(i_{\mathrm{a\_i}}d_{\mathrm{a\_i}} + i_{\mathrm{b\_i}}d_{\mathrm{b\_i}} + i_{\mathrm{c\_i}}d_{\mathrm{c\_i}}\right). \end{aligned} \tag{6}$$

Substituting (6) and the measured dc-link voltage into (2), the capacitance of the dc-link capacitor in traction inverters can be estimated by (7). It is worth noting that this capacitance estimation is implemented with the closed-loop current control on the dq-axis and requires only information on the dc-link voltage, three-phase stator current, and duty cycles, which all existing in the EV traction inverter, indicating that no additional software control and hardware measurements are required. In addition, the above estimation principle is applicable to discharge profiles with arbitrary rotor electrical angles, and the only difference is that the duty cycles in different space vector sectors are calculated by switching vector on-times in different combinations.

$$\begin{aligned} C &= \frac{i_{\mathrm{dis\_ave}} \triangle t}{\triangle v_{\mathrm{C}}} \\ &= \frac{(n-1)\,T_{\mathrm{S}}\sum_{i=1}^{n}\left(i_{\mathrm{a\_i}}d_{\mathrm{a\_i}} + i_{\mathrm{b\_i}}d_{\mathrm{b\_i}} + i_{\mathrm{c\_i}}d_{\mathrm{c\_i}}\right)}{n\left(v_{\mathrm{dc\_1}} - v_{\mathrm{dc\_n}}\right)} \end{aligned} \tag{7}$$

III. Error Analysis and Implementation Considerations

A. Sources of Estimation Error

In field applications, there could be considerable errors in the dc-link discharge profile, affecting the estimation accuracy. The errors in the measured dc-link voltage and three-phase stator current are mainly caused by system noise, sensors, analog-to-digital converters (ADCs) and, in particular, sampling asynchrony. From the above estimation principle, it is known that the dc-link voltage and stator currents should be sampled synchronously at the peak or valley of the PWM carrier at the switching frequency to obtain the required capacitor voltage and average stator currents. However, in practice, these sampling requirements could be difficult to fulfill as the inverter signals are typically measured asynchronously at a sampling rate up to the switching frequency for control purposes only, which implies that the sampling may occur in the vicinity of the peak or valley of the PWM carrier. These inherent system noise and unsatisfactory sampling conditions eventually cause random and bias errors in the measured electrical signals.

The duty cycles of the three-phase upper switches obtained from the controller of the traction inverter are mainly subject to bias errors. From (4) and (5), it is known that the duty cycles for estimating the average capacitor discharge current should correspond to the conduction times of the upper switches in a switching period, i.e., the time intervals during which the upper leg currents of the three-phase half-bridges are not zero. However, to prevent both upper and lower switches from conducting simultaneously, a dead time t_{d} is always inserted into the driving signals to implement break-before-make switching [26]. Moreover, the turn-ON and turn-OFF switching transients of power semiconductor switches are not ideal in practice. The dead time insertion and nonideal switching characteristics can lead to a bias error between the duty cycles calculated in the controller and the actual values, which seriously affects the estimation accuracy.

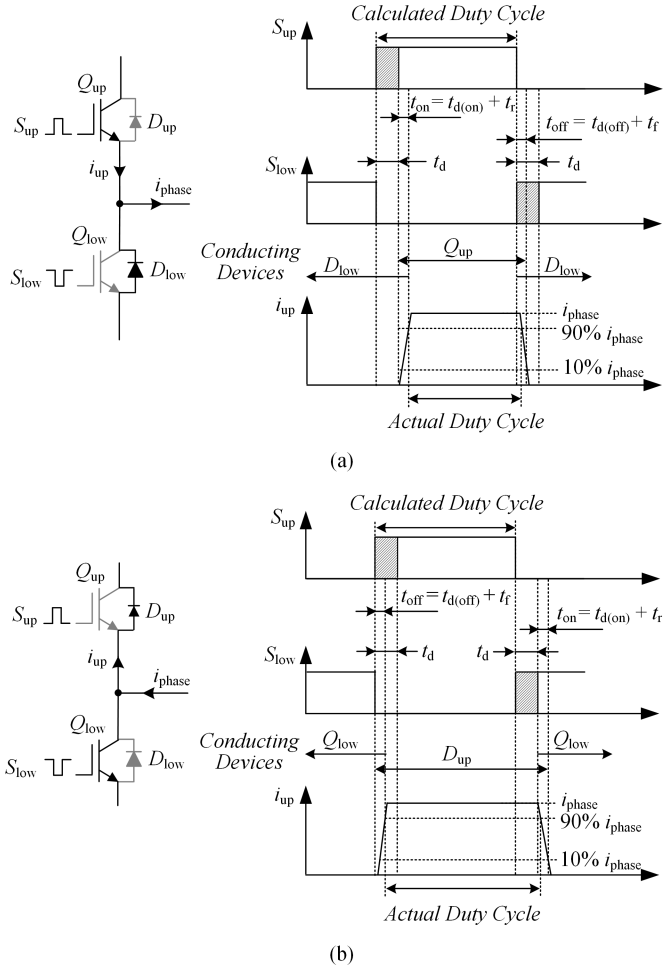

Fig. 4. Deviation between the duty cycle of the upper switch calculated in the controller and the actual duty cycle taking into account dead time insertion and non-ideal switching characteristics for a half-bridge circuit with (a) a forward phase current and (b) a reverse phase current in a switching period. i_{up} is the upper leg current, i_{phase} is the output phase current, and S_{up} and S_{low} are the driving signals of the upper and lower switches, respectively. t_{d} is the dead time. The turn-ON time t_{on} consists of the turn-ON delay time $t_{\mathrm{d(on)}}$ and the rise time t_{r}, and the turn-OFF time t_{off} consists of the turn-OFF delay time $t_{\mathrm{d(off)}}$ and the fall time t_{f}.

Fig. 4 illustrates the deviation of the calculated duty cycle of the upper switch from the actual value through the key waveforms of a half-bridge circuit with different phase current directions in a switching period, where the IGBT Q_{up} and free-wheeling diode D_{up} constitute the upper switch, and the lower switch consists of Q_{low} and D_{low}. S_{up} and S_{low} are the driving signals of the upper and lower switches, respectively. i_{up} is the upper leg current, and i_{phase} is the output phase current of the half-bridge circuit. The turn-ON time t_{on} consists of the turn-ON delay time $t_{\mathrm{d(on)}}$ and the rise time t_{r}, where the turn-ON

delay time $t_{\mathrm{d(on)}}$ corresponds to the time interval between the moment when the gate-emitter voltage has reached 10% of its end value and the collector current has increased to 10% of the phase current i_{phase}, and during the subsequent rise time t_{r}, the collector current increases from 10% to 90% of the phase current. The turn-OFF time t_{off} consists of the turn-OFF delay time $t_{\mathrm{d(off)}}$ and the fall time t_{f}, where the turn-OFF delay time $t_{\mathrm{d(off)}}$ is defined as the time interval between the moment when the gate-emitter voltage has dropped to 90% of its turn-ON value and the collector current has declined to 90% of the phase current. The fall time t_{f} is defined as the time interval during which the collector current drops from 90% to 10% of the phase current.

From Fig. 4(a), it can be seen that for the half-bridge with a forward phase current, the phase current i_{phase} flows through the upper IGBT Q_{up} and the lower free-wheeling diode D_{low} in a switching period. During the dead times, the current flow path is mainly provided by the lower free-wheeling diode D_{low}, while during the switching times t_{on} and t_{off}, the upper IGBT Q_{up} and the lower freewheeling diode D_{low} are both conducting. If the actual conduction time of the upper switch is defined as the time interval when the upper leg current i_{up} is greater than 90% of the phase current i_{phase}, the calculated duty cycle in the case of positive phase current deviates from the actual value by a dead time t_{d}, a turn-ON time t_{on}, and a turn-OFF delay time $t_{\mathrm{d(off)}}$. On the contrary, for the half-bridge with a reverse phase current shown in Fig. 4(b), the flow path of the phase current i_{phase} in a switching period is provided by the upper free-wheeling diode D_{up} and lower IGBT Q_{low}. The phase current mainly flows through the diode D_{up} during the dead times, while both D_{up} and Q_{low} during the switching times t_{on} and t_{off}. Hence, in the case of reverse phase current, the actual duty cycle of the upper switch is greater than the value calculated in the controller.

B. Error Correction for Practical Implementation

To ensure estimation accuracy in practical applications, the errors in the analog and digital signals for capacitance estimation should be eliminated as far as possible. The error in the measured dc-link voltage is generally negligible due to the high capacitor voltage drop over the estimation interval, but the errors in the measured stator currents and the calculated duty cycles cannot be neglected because the average capacitor discharge current is low.

The bias error in the measured stator currents is mainly caused by asynchronous sampling, resulting in a nonzero-sum of the three-phase current. Since the three-phase duty cycles are all around 50% during the dc-link discharge, as shown in Fig. 2, 0.5 times the nonzero current sum can be introduced into the calculated average discharge current, which could result in a considerable estimation error. To reduce the influence of the current asynchronous sampling, the average capacitor discharge current over the estimation interval is calculated through two-phase currents, as given in (8), where the subscripts x, y, and z can arbitrarily correspond to the phases a, b, c of the traction inverter. The two-phase calculation can effectively eliminate the current bias errors due to the extremely small terms $d_{\mathrm{x\_i}} - d_{\mathrm{z\_i}}$ and $d_{\mathrm{y\_i}} - d_{\mathrm{z\_i}}$.

$$i_{\mathrm{dis\_ave}} = \frac{1}{n}\sum_{i=1}^{n}\left[i_{\mathrm{x\_i}} * (d_{\mathrm{x\_i}} - d_{\mathrm{z\_i}}) + i_{\mathrm{y\_i}} * (d_{\mathrm{y\_i}} - d_{\mathrm{z\_i}})\right]. \tag{8}$$

The random errors in the stator currents and duty cycles can be eliminated by limiting the estimation interval within the discharge steady state, as labeled in Fig. 2. Since the three-phase stator current remains constant during the discharge steady state, the average discharge current over the steady state interval can be calculated by averaging the stator currents and duty cycles, as given in (9), where the random errors can be well averaging filtered. It is worth pointing out that a greater contribution of the averaging process is that it can effectively reduce the sampling requirements for stator currents, including sampling rate, position, synchronization, and accuracy, as verified by a case study in Section IV-B. The constant stator currents in the estimation interval imply that they can be measured asynchronously in the vicinity of the peak or valley of the PWM carrier with a sampling rate lower than the switching frequency, and the filtering function of the averaging process can also reduce the requirements for sensor accuracy and AD resolution.

$$\begin{aligned} i_{\mathrm{dis\_ave}} = {} & \frac{1}{n^2}\sum_{i=1}^{n} i_{\mathrm{x\_i}} * \sum_{i=1}^{n}(d_{\mathrm{x\_i}} - d_{\mathrm{z\_i}}) \\ & + \frac{1}{n^2}\sum_{i=1}^{n} i_{\mathrm{y\_i}} * \sum_{i=1}^{n}(d_{\mathrm{y\_i}} - d_{\mathrm{z\_i}}). \end{aligned} \tag{9}$$

The bias errors in the three-phase duty cycles obtained from the controller caused by dead time insertion and nonideal switching characteristics contribute to the estimation error to a considerable extent, which must be compensated with the dead time t_{d} and the switching times t_{on} and t_{off} according to the polarity of the corresponding phase current, as given in (10) shown at the bottom of the next page , where the actual conduction time of the upper switch is defined as the time interval when the upper leg current is greater than 50% of the phase current. The switching times can be obtained from the datasheet of the power semiconductor module, and the polarity of the three-phase stator current in the discharge can be known directly from the rotor electrical angle due to the monotonic dependence. Eventually, based on the above error correction scheme, the dc-link capacitance of the traction inverter can be accurately estimated by (11) shown at the bottom of the next page.

IV. Experimental Verification

A. Verification on a Scaled-Down Inverter Prototype

To verify the feasibility of the proposed capacitance estimation method, a scaled-down three-phase inverter prototype is built to simulate the EV traction inverters, as shown in Fig. 5(a), along with its hardware realization in Fig. 5(b). A dc power supply is connected to the dc-link of the three-phase inverter via a circuit breaker, and two film capacitors #1 and #2 of the same type (ELECTRONICON $^{\mathrm{TM}}$ PK16) but at different degradation levels are used alternatively for the dc-link design to emulate

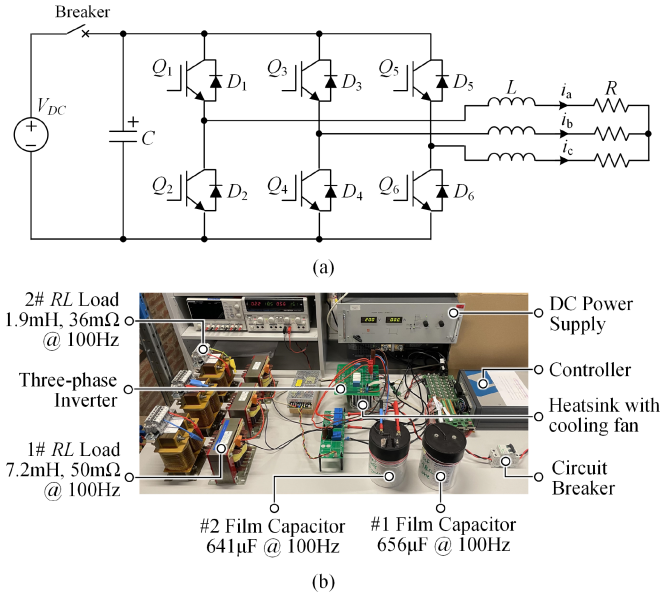

Fig. 5. Scaled-down three-phase inverter prototype for methodology validation. (a) Inverter topology. (b) Hardware realization.

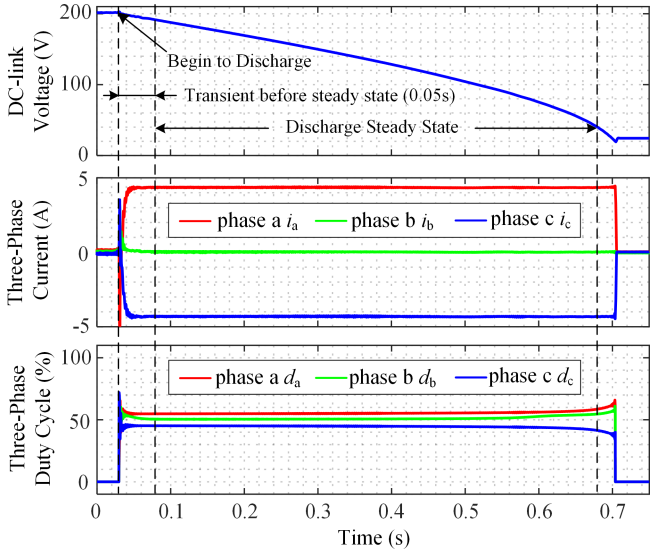

Fig. 6. Experimental discharge profile of the scaled-down inverter prototype with the #1 DC-link film capacitor, d-axis current reference $i_{\mathrm{d\_ref}}$ of 5 A, rotor electrical position θ_{e} of $\pi/6$, initial dc-link voltage V_{C0} of 200 V, heatsink temperature T_{H} of 25 °C, and RL load of 7.2 mH and 50 mΩ.

the degradation-induced capacitance drop in practice. The capacitance of the two film capacitors is measured by an *LCR* meter [27] at 100 Hz with the values of 656 and 641 μ F, respectively, where the capacitance difference is equivalent to a 2.3% drop. The power semiconductors adopt the IGBT module of Infineon FS25R12KT3 [28], which is mounted on an aluminum heatsink with a cooling fan and a temperature-controlled heating system. The same current control and modulation strategy as the EV traction inverter is implemented with a PLECS RT box, and the switching frequency is set at 10 kHz. The back-end motor stator windings are simulated by a three-phase RL load. Since the motor rotor is clamped during the dc-link discharge resulting in a zero back electromotive force, the load motor in this case can be equated to a three-phase RL load to some extent.

For the dc-link discharging operation mode of EV traction inverters, the main operating and environmental variables include the rotor electrical angle θ_{e}, the initial dc-link voltage V_{C0}, and the coolant temperature T_{C}, which are determined by the mission profile of the vehicle before shutdown and are random within a specific range. In addition, the equivalent impedance of the motor stator windings is current and temperature dependent and thus varies with the rotor electrical angle and coolant temperature. In the established scaled-down inverter prototype, the rotor electrical angle can be set arbitrarily in the controller (i.e., PLECS RT box) and the initial dc-link voltage is controlled by the dc power supply. The variations in coolant temperature and winding equivalent impedance are simulated by adjusting the heatsink temperature and connecting the #2 three-phase RL load in Fig. 5(b) in series on the load side, respectively.

Fig. 6 gives an experimental discharge profile of the inverter prototype with the discharge command $i_{\mathrm{d\_ref}}$ of 5 A, rotor electrical angle θ_{e} of $\pi/6$, initial dc-link voltage V_{C0} of 200 V, heatsink temperature T_{H} of 25 °C, and #1 RL load, where all electrical signals are sampled synchronously at the switching frequency of 10 kHz by sensors with a total error of $\pm 1\%$ and the duty cycles are obtained directly from the controller. It can be seen that the dc-link discharge starts at 0.03 s, followed by a gradual decrease in the dc-link voltage. The three-phase stator current reaches the steady state at 0.08 s after a short transient, and the duty cycles of the three-phase upper switches are maintained around 50% within the steady-state interval. The discharge is concluded when the dc-link voltage falls below 20 V, and then the discharge command $i_{\mathrm{d\_ref}}$ is reduced.

In the scaled-down discharge test, there is no bias error in the measured three-phase stator current due to synchronous sampling, but the bias error caused by dead time insertion and nonideal switching characteristics still exists in the duty cycles obtained from the controller. Fig. 7 gives the driving signal S_{a} of the phase a upper switch as well as the phase a output voltage v_{a} and current i_{a} in the dc-link discharge with rotor electrical angles of 0 and π, respectively. It can be seen that in the case of forward phase a current shown in Fig. 7(a), the phase a upper

$$d_{\mathrm{x/y/z\_i\_comp}} = \begin{cases} d_{\mathrm{x/y/z\_i}} - \frac{t_{\mathrm{d}}+t_{\mathrm{d(on)}}-t_{\mathrm{d(off)}}-0.5(t_{\mathrm{r}}-t_{\mathrm{f}})}{T_{\mathrm{S}}} & if\ i_{\mathrm{x/y/z\_i}} > 0 \\ d_{\mathrm{x/y/z\_i}} + \frac{t_{\mathrm{d}}+t_{\mathrm{d(on)}}-t_{\mathrm{d(off)}}-0.5(t_{\mathrm{r}}-t_{\mathrm{f}})}{T_{\mathrm{S}}} & if\ i_{\mathrm{x/y/z\_i}} < 0 \end{cases} \tag{10}$$

$$C = \frac{(n-1)\,T_{\mathrm{S}}}{n^2\,(v_{\mathrm{dc\_1}} - v_{\mathrm{dc\_n}})} \left[\sum_{i=1}^{n} i_{\mathrm{x\_i}} * \sum_{i=1}^{n} (d_{\mathrm{x\_i\_comp}} - d_{\mathrm{z\_i\_comp}}) + \sum_{i=1}^{n} i_{\mathrm{y\_i}} * \sum_{i=1}^{n} (d_{\mathrm{y\_i\_comp}} - d_{\mathrm{z\_i\_comp}}) \right]. \tag{11}$$

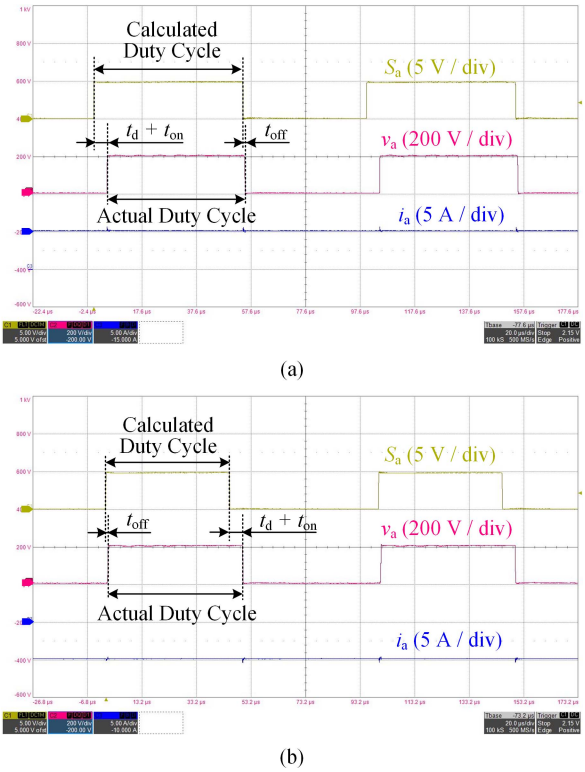

Fig. 7. Driving signal S_a of the phase a upper switch and the corresponding output phase voltage v_a and phase current i_a in the DC-link discharge with the rotor electrical angles of (a) 0 and (b) π, respectively.

switch is not turned on immediately after the driving signal S_a is enabled due to the dead time t_d and turn-ON time t_{on}, and it is turned OFF with a delay of a turn-OFF time t_{off}. The actual duty cycle of the upper switch is significantly less than the value calculated in the controller. On the contrary, in the case of reverse phase a current, the actual duty cycle of the upper switch is larger than the calculated value because the phase a upper free-wheeling diode remains conducting during the dead time t_d and the turn-ON time t_{on}, as shown in Fig. 7(b). Since these bias errors account for a considerable proportion of the actual duty cycle, the estimation accuracy can be severely deteriorated and corresponding compensation measures are essential.

To verify that the proposed method is feasible under variable operating and environmental conditions, the scaled-down discharge tests are performed under different conditions, as given in Table II, where the two film capacitors at different degradation levels are discharged 5 times each in each case. To secure the estimation accuracy, the capacitance values are estimated with the correction solutions given in Section III-B. Specifically, the estimation interval is limited within the period where the three-phase current remains in the steady state, as labeled in Fig. 6. In general, the transient process before the phase currents reach the steady state is extremely short, e.g., only 0.05 s in Fig. 6, and the discharge is concluded until the dc-link voltage drops to a low-amplitude safe voltage. Therefore, the estimation interval can be generally set to the interval, where the dc-link voltage v_{dc} drops from 90 % of its initial value to 100 V, and thus in this case study, the discharge profiles with v_{dc} drops from

TABLE II
OPERATING AND ENVIRONMENTAL CONDITIONS FOR THE SCALED-DOWN DC-LINK DISCHARGE TESTS

Case	θ_e	V_{C0}	T_H	RL Load	Discharge Times
1	π*1/6	200 V	25 °C	7.2 mH, 50 mΩ	5
2	π*3/6	200 V	25 °C	7.2 mH, 50 mΩ	5
3	π*5/6	200 V	25 °C	7.2 mH, 50 mΩ	5
4	π*7/6	200 V	25 °C	7.2 mH, 50 mΩ	5
5	π*9/6	200 V	25 °C	7.2 mH, 50 mΩ	5
6	π*11/6	200 V	25 °C	7.2 mH, 50 mΩ	5
7	π*1/6	250 V	25 °C	7.2 mH, 50 mΩ	5
8	π*1/6	200 V	25 °C	9.1 mH, 86 mΩ	5
9	π*1/6	200 V	50 °C	7.2 mH, 50 mΩ	5

180 V or 225 V to 100 V are utilized to estimate the capacitance value. The average discharge current over the estimation interval is calculated by averaging the phase currents and duty cycles, as given in (9), where the duty cycles are compensated with dead time and switching times according to the polarity of the phase currents, as given in (10).

Fig. 8(a) gives the estimated capacitance of the #1 and #2 film capacitors for the different test cases in Table II, where the nine test cases are represented by different colored markers and the discharge profiles for capacitance estimation are sampled at the switching frequency of 10 kHz. Considering that the sampling rate could be lower than the switching frequency in practical applications, the original discharge profiles are resampled at 1/10 and 1/100 of the switching frequency and the consequent estimation results are given in Fig. 8(b) and (c), respectively. The lower sampling rates are implemented by randomly selecting data within the corresponding sampling period from the original discharge profiles. From Fig. 8(a) and (b), it can be seen that the estimation results at the sampling rates of the switching frequency and the 1/10 of the switching frequency are in close agreement with the measurements of the *LCR* meter, and the estimation accuracy is barely affected by the operating and environmental conditions of the dc-link discharge. The maximum absolute estimation errors for #1 and #2 capacitors in the nine test cases are 6.4 and 6.1 μF, respectively, accounting for 0.98% and 0.95% of the measured values only. It is worth noting that the capacitance measured by the *LCR* meter at 100 Hz is a reference value here, which may have a little deviation from the actual capacitance value because the latter is operating condition dependent. In contrast to the estimation results at the above two sampling rates, the estimated capacitance at the sampling rate of 1/100 of the switching frequency given in Fig. 8(c) exhibits an irregular deviation from the measurements of the *LCR* meter, with part of the result clusters for the two capacitors are overlapped. This significant estimation error is mainly caused by: 1) due to the limited data collected at the low sampling rate, the random errors in phase currents and duty cycles cannot be well averaging filtered; 2) at the sampling rate of 1/100 of the switching frequency, the capacitance estimation based on (11) means that one collected data is used to approximate the average value over 100 switching periods. Since the three-phase duty cycles are only maintained at around 50% during the discharge steady

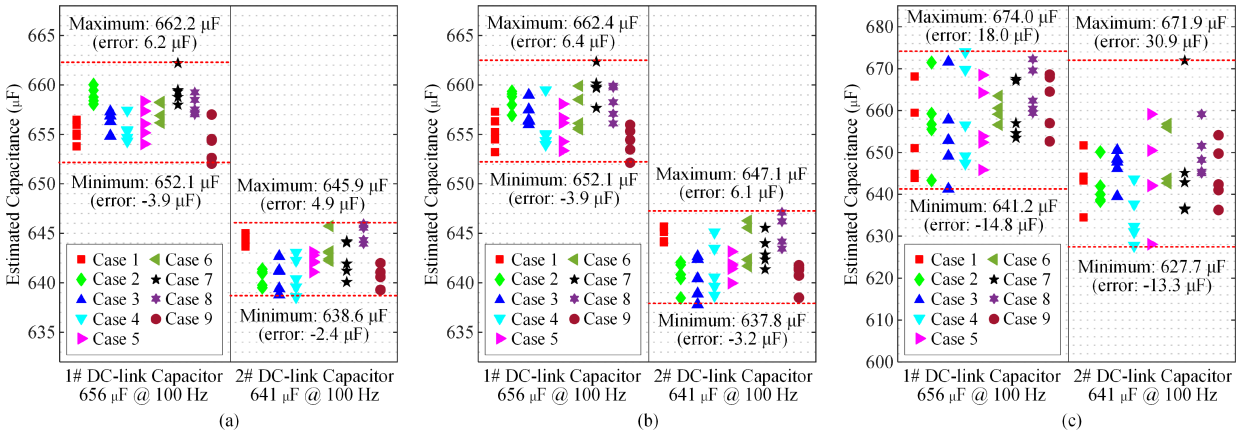

Fig. 8. Estimation results of the #1 and #2 DC-link film capacitors for the different test cases in Table II by means of the discharge profiles sampled at (a) the switching frequency of 10 kHz, (b) 1/10 of the switching frequency, and (c) 1/100 of the switching frequency, respectively.

TABLE III
ESTIMATION ERROR ANALYSIS FOR #1 AND #2 FILM CAPACITORS BASED ON THE MEAN AND 95 % CI OF THE ESTIMATION RESULTS AT DIFFERENT SAMPLING RATES

Sampling rate	Capacitor	Capacitance measured by LCR meter at 100 Hz (Capacitance drop %)	Estimated capacitance		Estimation error	
			Mean (Capacitance drop %)	95% CI	Mean	95% CI
Switching frequency of 10 kHz	#1	656 μF (0 %)	656.8 μF (0 %)	[652.7 μF 660.9 μF]	+ 0.8 μF	[-3.3 μF +4.9 μF]
	#2	641 μF (2.3 %)	642.2 μF (2.2 %)	[638.2 μF 646.2 μF]	+ 1.2 μF	[-2.8 μF +5.2 μF]
1/10 of the switching frequency	#1	656 μF (0 %)	656.9 μF (0 %)	[652.4 μF 661.3 μF]	+ 0.9 μF	[-3.6 μF +5.3 μF]
	#2	641 μF (2.3 %)	642.5 μF (2.2 %)	[637.8 μF 647.1 μF]	+ 1.5 μF	[-3.2 μF +6.1 μF]
1/100 of the switching frequency	#1	656 μF (0 %)	658.7 μF (0 %)	[641.7 μF 675.7 μF]	+ 2.7 μF	[-14.3 μF +19.7 μF]
	#2	641 μF (2.3 %)	644.8 μF (2.1 %)	[627.6 μF 661.9 μF]	+ 3.8 μF	[-13.4 μF +20.9 μF]

state rather than being constant, this approximation can lead to considerable errors. Therefore, for the proposed capacitance estimation method, it is recommended that the sampling rate should not be less than 1/10 of the switching frequency.

Due to the limited test scenarios and times, the estimation results for each film capacitor at a specific sampling rate in Fig. 8 are treated as one data cluster (i.e., the nine test cases in Table II are no longer differentiated) and the probability density distributions of the total of six data clusters are analyzed. Table III gives the mean and 95% confidence interval (CI) for each estimation result cluster, as well as the corresponding estimation error relative to the measurements of the *LCR* meter. It can be seen that at the sampling rate of the switching frequency and 1/10 of the switching frequency, the 95 % CIs for #1 and #2 capacitors are narrow with the widest ranges of [652.4 μF 661.3 μF] and [637.8 μF 647.1 μF], respectively. Relative to the measurements of the *LCR* meter, the maximum absolute estimation errors for the two capacitors at the 95% confidence level are 5.3 and 6.1 μF only, accounting for 0.8% and 1.0% of the measured value. This indicates that the proposed method is capable of producing accurate capacitance estimations with a high degree of confidence at these sampling rates, and the variability and uncertainty in the estimation are low. In contrast, at the sampling rate of 1/100 of the switching frequency, the 95 % CI becomes wide and the maximum absolute estimation errors for #1 and #2 capacitors at the 95 % confidence level reaches 19.7 and 20.9 μF, respectively, accounting for 3.0% and 3.3% of the measured values of the *LCR* meter. However, it is worth stating that in practice, a primary application of the capacitance estimation is the health and condition monitoring of capacitors, which is typically implemented with the capacitance drop in terms of percentage, e.g., the typical end-of-life criteria for film capacitors is a 5% drop in capacitance [3]. In such a case, if the average value of the estimation results is used for health assessment, it is possible to distinguish the degradation-induced decrease in capacitance even at a low sampling rate. As given in Table III, the capacitance of the #2 capacitor measured by the LCR meter decreases by 2.3% compared to that of the #1 capacitor, while the drop percentages between the mean of the estimation results of these two capacitors at the sampling rate of 1/100 of the switching frequency is 2.1%, with a deviation of 0.2% only. Therefore, in practical implementations, even if the sampling rate is much lower than the switching frequency, the proposed scheme can still potentially be used for health monitoring purposes by averaging the estimation results collected over a period of time.

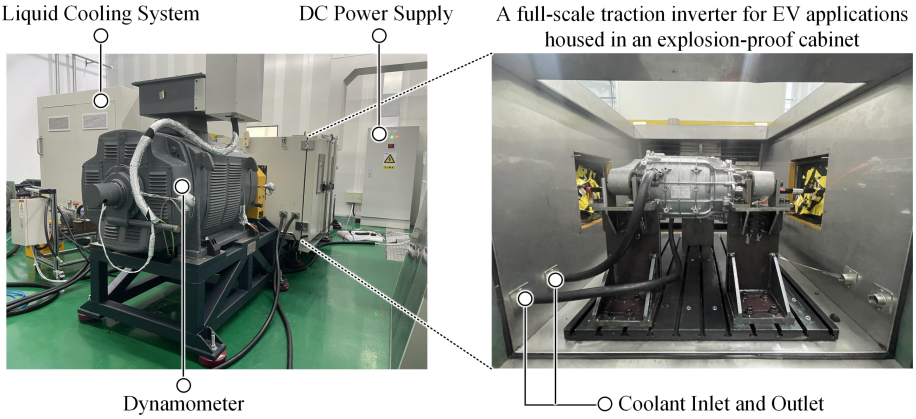

Fig. 9. Experimental platform with a full-scale traction inverter for EV applications.

B. Verification on a Full-Scale EV Traction Inverter

To verify the feasibility of the proposed estimation method in practical applications, the dc-link discharge tests are performed on a full-scale traction inverter for EV applications with a continuous power rating of 160 kW and a continuous torque of 305 N·m, as shown in Fig. 9. A high-voltage dc power supply is connected to the dc-link of the traction inverter via a circuit breaker to simulate the battery pack, and the traction inverter is housed in an explosion-proof cabinet for safety reasons. The full-scale traction inverter is mainly composed of a customized dc-link metalized polypropylene film capacitor from Xiamen Faratronic Co. Ltd., an IGBT power module of Infineon FS820R08A6P2B [29], a controller, and a liquid cooling system, and also integrates a squirrel-cage asynchronous motor whose rotor is connected to a dynamometer in Fig. 9. The switching frequency is set at 10 kHz with a symmetrical space vector PWM. Due to the lack of degraded samples, the degradation-induced decrease in capacitance in the full-scale discharge tests is indirectly emulated by increasing the coolant temperature. The capacitance value of the dc-link capacitor measured by an *LCR* meter [27] at 100 Hz with the coolant temperature of 25 °C, 55 °C, and 85 °C are 357.1 μF, 352.6 μF, and 347.0 μF, respectively. This implies that if the dc-link capacitor at the coolant temperature of 25 °C is considered to be in a healthy state, the capacitor at the coolant temperatures of 55 °C and 85 °C can be regarded as being in a degraded state with a 1.3% and 2.8% capacitance drop, respectively.

Fig. 10(a) gives an experimental discharge profile of the full-scale traction inverter with the rotor electrical angle of 1.1π, initial dc-link voltage of 350 V, coolant temperature of 25 °C, and d-axis current reference of 100 A, where all analog and digital information is obtained directly from the existing data acquisition system of the traction inverter. The sampling rate is set to 1 kHz, 10 times lower than the switching frequency, and the dc-link voltage and three-phase stator current are sampled asynchronously in the vicinity of the peak of the PWM carrier by sensors with a total error of ± 2 % and ADCs with 12-bit resolution. It can be seen that the circuit breaker is opened at 0.005 s to isolate the traction inverter from the power supply, and the subsequent discharge behavior is consistent with the scaled-down profile shown in Fig. 6. The measured three-phase stator current and their sum during the discharge steady state is given in Fig. 10(b), where the current fluctuations and the nonzero current sum indicate that there are measurement-induced random errors as well as bias errors caused by asynchronous current sampling, respectively. Therefore, to ensure estimation accuracy, it is essential to limit the estimation interval to the steady state for averaging processing and calculate the average discharge current by two-phase currents. In this case study, the estimation procedure follows the solution given in Section III-B, and the estimation interval is limited to the interval where the dc link voltage drops from 90% of its initial value to 100 V.

TABLE IV
OPERATING AND ENVIRONMENTAL CONDITIONS OF THE FULL-SCALE DC-LINK DISCHARGE TESTS

Case	T_C	θ_e	V_{C0}	Discharge Times
1	25 °C	1.1π	400 V	5
2	25 °C	1.1π	300 V	5
3	25 °C	0.4π	300 V	5
4	55 °C	1.1π	400 V	5
5	55 °C	1.1π	300 V	5
6	55 °C	0.4π	300 V	5
7	85 °C	1.1π	400 V	5
8	85 °C	1.1π	300 V	5
9	85 °C	0.4π	300 V	5

The operating and environmental conditions of the full-scale dc-link discharge test are given in Table IV, where each case contains five discharge profiles at the same test conditions. The initial dc-link voltage V_{C0} is determined according to the normal operating voltage range of the battery pack in EVs from 250 to 430 V, and the changes in coolant temperature T_C can change both the impedance of the motor stator windings and the capacitance of the dc-link capacitor. Before the discharge tests at each temperature level, the coolant temperature is stabilized at the target temperature for 2 h. Since the backside of the customized dc-link capacitor is provided with a cooling surface connected to the liquid cooling channel surface via thermal interface material, this time interval is sufficient for the internal and external temperatures of the capacitor to stabilize and align with the coolant temperature. The estimation results for different test

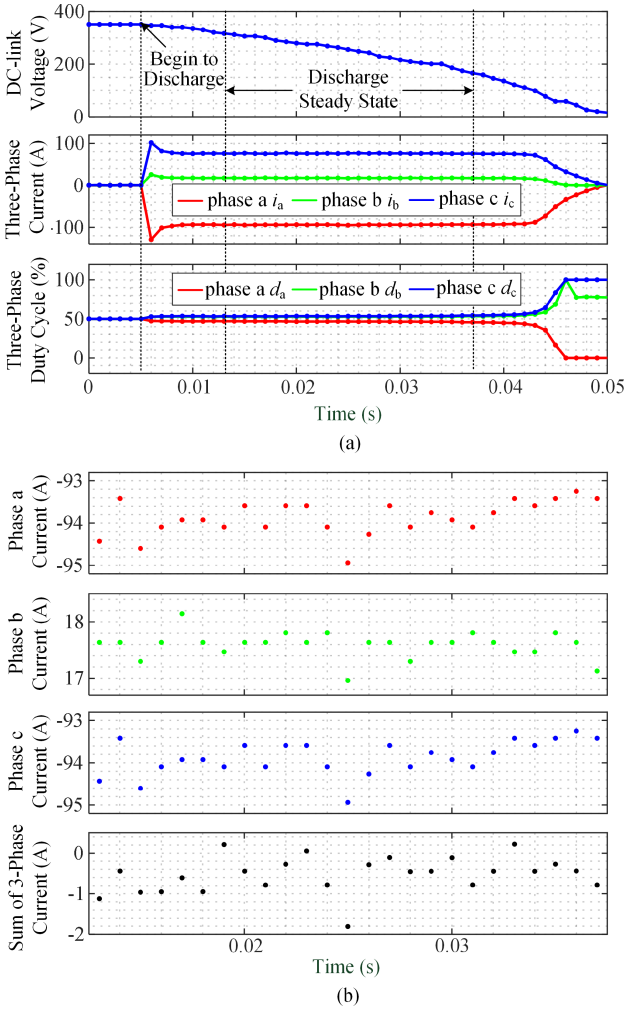

Fig. 10. DC-link discharge test of the full-scale traction inverter with the discharge command $i_{\mathrm{d\_ref}}$ of 100 A, rotor electrical angle θ_{e} of 1.1π, initial dc-link voltage V_{C0} of 350 V, and coolant temperature T_{C} of 25 °C. (a) Discharge profile with a sampling rate of 1 kHz. (b) Three-phase stator currents and their sum during the discharge steady state.

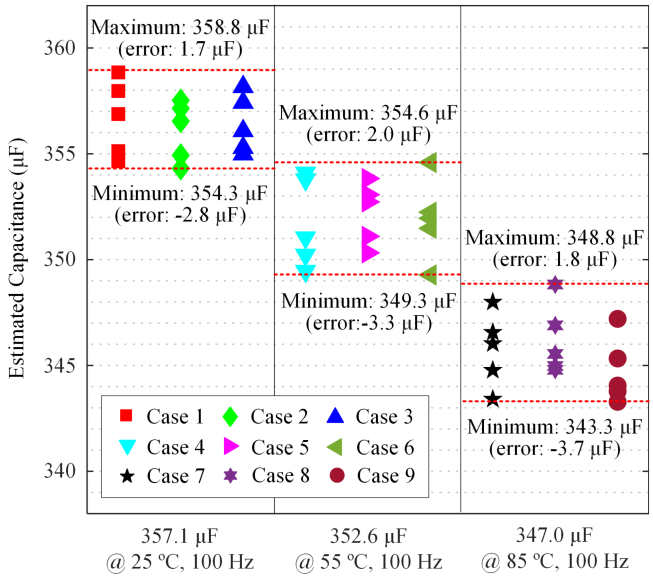

Fig. 11. Estimation results of the full-scale traction inverter for the different test cases in Table IV through the discharge profiles sampled at 1 kHz.

TABLE V
ESTIMATION ERROR ANALYSIS FOR FULL-SCALE DC-LINK CAPACITOR BASED ON THE MEAN AND 95 % CI OF THE ESTIMATION RESULTS AT DIFFERENT COOLANT TEMPERATURES

Coolant temperature	LCR measurements at 100 Hz (drop %)	Estimated capacitance		Estimation error	
		Mean (drop %)	95% CI	Mean	95% CI
25 °C	357.1 μF (0 %)	356.4 μF (0 %)	[353.6 μF 359.2 μF]	- 0.7 μF	[-3.5 μF +2.1 μF]
55 °C	352.6 μF (1.3 %)	352.0 μF (1.3 %)	[348.6 μF 355.3 μF]	- 0.6 μF	[-4.0 μF +2.7 μF]
85 °C	347.0 μF (2.8 %)	345.6 μF (3.0 %)	[342.3 μF 348.8 μF]	-1.4 μF	[-4.7 μF +1.8 μF]

cases are given in Fig. 11, where the nine cases are represented by different colored markers, and the same colored markers represent the distribution of the estimation results in the same case.

From Fig. 11, it can be seen that even though the sampling rate is at 1/10 of the switching frequency, the estimated capacitance still exhibits a high-level agreement with the values measured by the *LCR* meter, and the estimation accuracy is independent of changes in operating and environmental conditions, which are consistent with the scaled-down experimental results. Compared to the measurements of the *LCR* meter, the maximum absolute estimation error is 3.7 μF only, accounting for 1.1% of the measured value. By analyzing the probability density distributions of the estimation result clusters at different coolant temperatures, the mean value and 95% CI for each result cluster, as well as the errors relative to the measurements of the *LCR* meter, are given in Table V. It can be seen that the 95% CI remains narrow at different coolant temperature levels and the maximum absolute estimation error at the 95% confidence level is 4.7 μF, accounting for 1.4% only of the *LCR* measurement. This demonstrates that the proposed capacitance estimation method can still provide accurate estimation with high confidence in a real traction inverter. Furthermore, in the full-scale discharge test, the degradation-induced decrease in capacitance is indirectly emulated by increasing the coolant temperature. The drop percentage between the mean values of the estimated result clusters at different coolant temperature levels given in Table V indicates that this capacitance drop can be well identified.

Table VI gives a comprehensive comparison of the proposed estimation method with the existing schemes in terms of cost, complexity, safety, and estimation accuracy. As with most existing schemes based on discharge profiles, since the estimation is performed after the system is shut down and is implemented with the existing information of traction inverters, the proposed method does not interfere with normal operation and is cost-effective without additional sensors. However, the

TABLE VI
COMPREHENSIVE COMPARISON OF THE PROPOSED METHOD WITH EXISTING CAPACITANCE ESTIMATION SCHEMES

Method		Cost	Complexity	Risk	Accuracy
Capacitor ripple-based methods	[12]	++	+++	+++	≤ 1.0 % (a)
	[13],[14]	+	+++	++	≤ 5.4 % (a)
External signal injection-based methods	[15],[16]	+	+++	+++	≤ 1.4 % (a)
	[17]	+	+++	+++	≤ 1.0 % (a)
Discharge/charge profile-based methods	[18]	+++	+	+	≤ 2.5 % (a) ≤ 2.3 % (b)
	[19]	+++	+++	+	≤ 1.1 % (a)
	[20]	+	+++	+	≤ 5.1 % (a)
	[21],[22]	+	+++	+	≤ 2.0 % (a) ≥ 5.0 % (b)
	Proposed method	+	+	+	≤ 1.1 % (b)

(a): Accuracy derived from experimental results in the relevant literature
(b): Accuracy derived from experimental results on the full-scale test platform in this paper

difference is that the sampling requirements of the proposed method are much lower without the need to update the existing measurement platform. In addition, the estimation accuracy in field applications can be guaranteed contributed by the proposed error correction solution. The schemes proposed in [18], [21], [22] are also implemented on the full-scale test platform of this article, and the accuracy derived from the experimental results for these schemes is given in Table VI. It can be noted that the accuracy of the proposed scheme is relatively high in this case study. In summary, the proposed method is easier to implement and more accurate, which is expected to be implemented in real EV traction inverters.

V. CONCLUSION

This article presents a dc-link capacitance estimation method for EV traction inverters, aiming to facilitate the practical implementation of health and condition monitoring for dc-link capacitors. It is achieved by leveraging the discharge profile of the inverter dc-link capacitor after the vehicle is shut down and can be implemented with the existing current control and sensors of traction inverters without software or hardware intrusion. Compared with existing schemes, the proposed method has the advantages of: 1) it has low sampling requirements and is therefore easy to implement without the need for upgrades of existing measurement platforms; 2) it can effectively eliminate and compensate for errors in discharge profiles, thus guaranteeing the estimation accuracy in field applications. The experimental results prove the feasibility of the proposed method on both a scaled-down inverter prototype and a full-scale EV traction inverter, and the estimation errors at 95 % confidence level, under complex operating and environmental conditions and moderate sampling conditions, are limited to 1.0% and 1.4%, respectively, which are sufficient for health assessment purposes.

It is worth stating that the proposed capacitance estimation method is also applicable to traction inverters where the dc-link is designed with aluminum electrolytic capacitors. In addition, in some traction inverters, there could be an active discharge path consisting of power devices and resistors in parallel with the dc-link, and the dc-link capacitor is discharged through both the motor stator windings and the resistors. In this situation, the current in the active discharge path needs to be taken into account in the calculated average discharge current, which can be derived from the measured dc-link voltage.

REFERENCES

[1] H. Wang, H. Wang, G. Zhu, and F. Blaabjerg, "An overview of capacitive DC-links-topology derivation and scalability analysis," *IEEE Trans. Power Electron.*, vol. 35, no. 2, pp. 1805–1829, Feb. 2020.

[2] H. Wen, W. Xiao, X. Wen, and P. Armstrong, "Analysis and evaluation of DC-link capacitors for high-power-density electric vehicle drive systems," *IEEE Trans. Veh. Technol.*, vol. 61, no. 7, pp. 2950–2964, Sep. 2012.

[3] H. Wang and F. Blaabjerg, "Reliability of capacitors for DC-link applications in power electronic converters–an overview," *IEEE Trans. Ind. Appl.*, vol. 50, no. 5, pp. 3569–3578, Sep./Oct. 2014.

[4] H. Wang, P. Davari, H. Wang, D. Kumar, F. Zare, and F. Blaabjerg, "Lifetime estimation of DC-link capacitors in adjustable speed drives under grid voltage unbalances," *IEEE Trans. Power Electron.*, vol. 34, no. 5, pp. 4064–4078, May 2019.

[5] F. Blaabjerg, H. Wang, I. Vernica, B. Liu, and P. Davari, "Reliability of power electronic systems for EV/HEV applications," *Proc. IEEE*, vol. 109, no. 6, pp. 1060–1076, Jun. 2021.

[6] B. Yao et al., "Accelerated degradation testing and failure mechanism analysis of metallized film capacitors for AC filtering," *IEEE Trans. Power Electron.*, vol. 39, no. 5, pp. 6256–6270, May 2024.

[7] H. Wang, M. Liserre, and F. Blaabjerg, "Toward reliable power electronics: Challenges, design tools, and opportunities," *IEEE Ind. Electron. Mag.*, vol. 7, no. 2, pp. 17–26, Jun. 2013.

[8] J. Falck, C. Felgemacher, A. Rojko, M. Liserre, and P. Zacharias, "Reliability of power electronic systems: An industry perspective," *IEEE Ind. Electron. Mag.*, vol. 12, no. 2, pp. 24–35, Jun. 2018.

[9] S. Yang, A. Bryant, P. Mawby, D. Xiang, L. Ran, and P. Tavner, "An industry-based survey of reliability in power electronic converters," *IEEE Trans. Ind. Appl.*, vol. 47, no. 3, pp. 1441–1451, May/Jun. 2011.

[10] Y. Avenas, L. Dupont, N. Baker, H. Zara, and F. Barruel, "Condition monitoring: A decade of proposed techniques," *IEEE Ind. Electron. Mag.*, vol. 9, no. 4, pp. 22–36, Dec. 2015.

[11] Z. Zhao, P. Davari, W. Lu, H. Wang, and F. Blaabjerg, "An overview of condition monitoring techniques for capacitors in DC-link applications," *IEEE Trans. Power Electron.*, vol. 36, no. 4, pp. 3692–3716, Apr. 2021.

[12] P. Sundararajan et al., "Condition monitoring of DC-link capacitors using goertzel algorithm for failure precursor parameter and temperature estimation," *IEEE Trans. Power Electron.*, vol. 35, no. 6, pp. 6386–6396, Jun. 2020.

[13] L. A. Rodrigues, V. Junior De Paris, A. S. Vaccari, and G. Waltrich, "Real time measurements of aluminum electrolytic capacitor parameters in EVs inverters," in *Proc. IEEE Energy Convers. Congr. Expo.*, Nashville, TN, USA, 2023, pp. 3495–3502.

[14] W. Zhang, Y. He, X. Wang, and J. Chen, "A comprehensive method for online switch fault diagnosis and capacitor condition monitoring of three-level T-type inverters," *IEEE Trans. Power Electron.*, vol. 38, no. 8, pp. 10183–10195, Aug. 2023.

[15] W. Zhou, M. Wang, and Q. Wu, "A model-based monitoring method for offline accelerated testing of DC-link capacitor in three-phase inverter systems," *IEEE Trans. Power Electron.*, vol. 36, no. 1, pp. 61–67, Jan. 2021.

[16] B. Guan and X. Zhen, "Noninvasive online capacitor monitoring method for three-level converter based on active neutral-point current adjustment," *IEEE Trans. Ind. Electron.*, vol. 71, no. 5, pp. 4320–4329, May 2024.

[17] T. Meng and P. Zhang, "An online DC-link capacitance estimation method for motor drive systems based on an intermittent reverse-charging control strategy," *IEEE Trans. Power Electron.*, vol. 38, no. 2, pp. 2481–2492, Feb. 2023.

[18] Y. Wu and X. Du, "A VEN condition monitoring method of DC-link capacitors for power converters," *IEEE Trans. Ind. Electron.*, vol. 66, no. 2, pp. 1296–1306, Feb. 2019.
[19] B. Wang, J. Meng, and P. Zhao, "Aging condition monitoring for aluminum electrolytic capacitor in variable speed drives," *IEEE Trans. Power Electron.*, vol. 37, no. 4, pp. 4564–4574, Apr. 2022.
[20] H. Li, D. Xiang, X. Han, X. Zhong, and X. Yang, "High-accuracy capacitance monitoring of DC-link capacitor in VSI systems by LC resonance," *IEEE Trans. Power Electron.*, vol. 34, no. 12, pp. 12200–12211, Dec. 2019.
[21] M. Kim, S.-K. Sul, and J. Lee, "Condition monitoring of DC-link capacitors in drive system for electric vehicles," in *Proc. IEEE Veh. Power Propulsion Conf.*, 2012, pp. 633–637.
[22] T. Meng and P. Zhang, "A novel non-invasive DC-link capacitance estimation method for motor drive system," in *Proc. IEEE 9th Int. Power Electron. Motion Control Conf.*, Nanjing, China, 2020, pp. 927–934.
[23] J. Reimers, L. Dorn-Gomba, C. Mak, and A. Emadi, "Automotive traction inverters: Current status and future trends," *IEEE Trans. Veh. Technol.*, vol. 68, no. 4, pp. 3337–3350, Apr. 2019.
[24] X. Wei, L. Jin, B. Yao, Y. Peng, and H. Wang, "Application-driven data acquisition for condition monitoring of power semiconductors in traction inverter applications," *IEEE Trans. Transp. Electrific.*, early access, doi: 10.1109/TTE.2023.3339848.
[25] D. Xie, C. Lin, H. Lin, W. Liu, Y. Du, and T. Basler, "OC switch fault diagnosis, pre- and postfault DC voltage balancing control for a CHBMC using SVM concept," *IEEE Trans. Power Electron.*, vol. 39, no. 1, pp. 677–692, Jan. 2024.
[26] H. Lin, C. Cai, J. Chen, Y. Gao, S. Vazquez, and Y. Li, "Modulation and control independent dead-zone compensation for h-bridge converters: A simplified digital logic scheme," *IEEE Trans. Ind. Electron.*, early access, doi: 10.1109/TIE.2024.3370975.
[27] "E4980 A precision LCR meter," Keysight, Tech. Rep. [Online]. Available: https://www.keysight.com/us/en/assets/7018-01355/data-sheets/5989-4435.pdf
[28] "IGBT module FS25R12KT3," Infineon, Tech. Rep. [Online]. Available: https://www.infineon.com/dgdl/Infineon-FS25R12KT3-DS-v02_01-en_de.pdf?fileId=db3a304412b407950112b431414d53ef
[29] "IGBT module FS820R08A6P2B," Infineon, Tech. Rep. [Online]. Available: https://www.infineon.com/dgdl/Infineon-FS820R08A6P2B-DataSheet-v03_01-EN.pdf?fileId=5546d4625fe36784015fe7bf8e872948

Xing Wei (Student Member, IEEE) received the B.E. degree in electrical engineering and automation from the Nanjing Normal University, Nanjing, China, in 2016, and the M.E. degree in electrical engineering from Southeast University, Nanjing, China, in 2019. He is currently working toward the Ph.D. degree in power electronic with Aalborg University, Aalborg, Denmark.

From 2017 to 2018, he was a Visiting Student with RWTH Aachen University, Aachen, Germany. He is a Research Assistant with Southeast University, Nanjing, China. His research interests include health and condition monitoring of traction inverters for electric vehicles.

Bo Yao (Graduate Student Member, IEEE) received the B.Eng. and M.Eng. degrees in electrical engineering from Southwest Jiaotong University (SWJTU), Chengdu, China, in 2017 and 2020, respectively, and the Ph.D. degree in power electronic from Department of Energy, Aalborg University, Aalborg, Denmark, in 2023.

He was seconded as a Visiting Scholar with the ABB Corporate Research Center, Vasteras, Sweden, from August to September 2023. He is currently engaged in postdoctoral research with the Energy Department of Aalborg University. His research interests include reliability testing, lifetime evaluation and condition monitoring of power electronic components in power converter systems.

Dr. Yao was a recipient of the Best Paper Award of IEEE International Conference on Electrical Machines and Systems (ICEMS) in 2019, and the SEMIKRON Young Engineer Award from the European Center for Power Electronics (ECPE) and SEMIKRON Foundation in 2023.

Yingzhou Peng (Senior Member, IEEE) received the B.S. degree in electrical engineering from Harbin Engineering University, Harbin, China, in 2014, the M.S. degree in power electronics from Chongqing University, Chongqing, China, in 2017, and the Ph.D. degree in power electronics from Aalborg University, Aalborg, Denmark in 2020.

From 2020 to 2022, He was a PosDoc with Aalborg University, Aalborg, Denmark. He was a Visiting Researcher with the Electrical Power and Energy Conversion Lab, Cambridge University, Cambridge, U.K, in 2020. He is currently working as an Assistant Professor with Hunan Unversity, China. His research interests include the failure mechanisms analysis of power electronic components, the improvement of the robustness and reliability of power converters by means of condition monitoring.

Yongchao Sun received the B.E degree in vehicle engineering from Dalian University of Technology, Dalian, China, in 2014.

He is currently working for NIO on area of electric motor control, health and condition monitoring of traction inverters.

Kai Wang (Member, IEEE) received the B.S. degree in electrical engineering from Zhejiang University, Hangzhou, China, in 2009, and the Ph.D. degree in electrical engineering from Zhejiang University, Hangzhou, China, in 2014.

From July 2014, he was with Eaton Corporate Research and Technology Centre, Shanghai, China, where he is a Lead Engineer with the Division of Power Systems and Architectures, responsible for generating innovative ideas, identifying market opportunities, evaluating and inventing new technologies, and developing business cases. Since April 2016, he has been with NIO Company Ltd., Shanghai, China, where he is currently now an Application Software Director and Technical Expert with Electric Drive System Department. He has been authored or coauthored more than 10 published technical papers and the holder of more than 60 international patents. His research interests include electric vehicle (EV) motion control systems, power electronics & motor control drives, and industrial digitization with AI technology applications.

He was a recipient of the first prize for China Automotive Industry Science and Technology Progress Award in 2021.

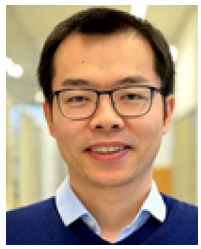

Huai Wang (Senior Member, IEEE) received the B.E. degree in electrical engineering from Huazhong University of Science and Technology, Wuhan, China, in 2007, and the Ph.D. degree in power electronics from the City University of Hong Kong, Hong Kong, in 2012.

He is currently a Professor with AAU Energy, Aalborg University, Denmark, where he leads the group of Reliability of Power Electronic Converters (ReliaPEC) and the mission on Digital Transformation and AI. He was a Visiting Scientist with the ETH Zurich, Switzerland, from Aug. to Sep. 2014, and with the Massachusetts Institute of Technology (MIT), USA, from September to November 2013. He was with the ABB Corporate Research Center, Switzerland, in 2009. His research addresses the fundamental challenges in modeling and validating power electronic component failure mechanisms and application issues in system-level predictability, condition monitoring, circuit architecture, and robustness design.

Dr. Wang received the Richard M. Bass Outstanding Young Power Electronics Engineer Award from the IEEE Power Electronics Society in 2016 and the 1st Prize Paper Award from IEEE TRANSACTIONS ON POWER ELECTRONICS in 2021. He serves as an Associate Editor for the *Journal of Emerging and Selected Topics in Power Electronics* and IEEE TRANSACTIONS ON POWER ELECTRONICS. He was elected as a member of the Danish Academy of Technical Sciences in 2023.